Quantitative assessment of femtosecond laser-induced stress waves in fused silica

Olga Koritsoglou, Guillaume Duchateau, Olivier Utéza, Alexandros Mouskeftaras

Quantitative Assessment of Femtosecond Laser-Induced Stress Waves in Fused Silica

Olga Koritsoglou[1], Guillaume Duchateau[2], Olivier Utéza[1] and Alexandros Mouskeftaras[1]

1. Aix-Marseille Université, CNRS, LP3, UMR7341, 13009 Marseille, France

2. CEA-CESTA, 15 Avenue des Sablières, CS60001, 33116 Le Barp Cedex, France

Abstract: Controlled processing of transparent materials with ultrashort laser pulses requires a detailed and precise knowledge of the various laser-matter interaction mechanisms from laser energy deposition and conversion in internal energy of the material to hydrodynamic relaxation and mechanical response. To address this issue, we first develop a multi-timescale experimental approach based on a femtosecond pump-and-probe microscope-polariscope. The pump is a 360-fs, 1-μJ infrared (1030 nm) laser pulse which is split to provide a 515-nm femtosecond probe with delay adjustable from femtoseconds to nanoseconds. The obtained time-resolved shadowgraphy images allow measurement of the transient probe transmission. Then, the carrier density is determined by use of the Beer-Lambert law and Drude model approach demonstrating the ultrafast formation of a slightly overcritical plasma inside the bulk of fused silica. In parallel, quantitative birefringence images provide a measurement of stress by use of the photoelastic law revealing the partial dissipation of the absorbed laser energy through emission of a GPa-stress wave, a few hundreds of picoseconds after the laser pulse. A multiscale-multiphysics model is then used to interpret the experimental observations, accounting for the electron dynamics, laser propagation and the hydrodynamic response. Following experimental validation, simulations allow determining the temporal evolution of local fundamental material properties (stress, density and temperature). This combination of experimental and simulation results enables us to quantitatively discuss the importance of the different laser energy relaxation channels in the material uncovering the full scenario of the interaction. Our model predicts a 20-GPa maximum initial stress loading with maximum lattice temperatures reaching 3.5 10^4 K. We also show that a fraction of ~2% of the total absorbed laser energy is dissipated through emission of a weak shockwave. Our approach could be used in the future to account for mechanically-driven transparent material structuring induced by ultrashort laser pulses.

I. Introduction

Femtosecond lasers allow reaching high optical intensities (in the TW/cm^2 range) with modest nanojoule laser pulse energies. At such intensities the interaction of the laser field with matter is highly nonlinear allowing processing of transparent materials with unsurpassed quality [1,2]. This unique feature facilitates three-dimensional writing inside transparent materials, serving as a foundation for the microfabrication of monolithic microsystems. Applications include optofluidic biochips [3], optical memories [4] and other lab-on-a-chip-based devices [5]. Equally important are applications of fundamental interest, such as laser-driven polymorphic transitions of materials [6], generation of high-order harmonics in transparent solids [7], and laser amplification in photo-excited materials such as fused silica (SiO_2) and sapphire [8].

The above-mentioned applications result from a complex, multiscale and multiphysical interaction of femtosecond laser pulses with matter [9,10]. Starting at the femtosecond timescale, the intense laser field is responsible for the photoionization of band gap materials such as fused silica. Then, the generated free-carrier population linearly absorbs the laser energy during the laser pulse by inverse Bremsstrahlung. At this stage, inelastic scattering of high-energy electrons may multiply the free-carrier density by impact ionization which in turn enhances optical absorption of the remaining laser pulse energy. In the same time, the laser propagation is modified due to variations of the dielectric permittivity induced by electron excitation. The laser-heated electron population further relaxes, progressively determining on the sub-picosecond timescale a Fermi-Dirac distribution centered on a few eV average temperature in such operating conditions. While electron transport is largely inhibited in dielectrics, the energy transfer from the electronic subsystem towards the lattice locally sets in, this process being complete at the picosecond timescale. Later, from sub-nanosecond to nanosecond timescales, hydrodynamic relaxation takes place including shock/stress wave emission and heat diffusion, with characteristic time of heat energy fully diffused outside the focal volume at the microsecond timescale. Depending on laser irradiation conditions, the material ultimately finds its final state and may be irreversibly modified. At all stages, the dielectric permittivity of the medium is changed enabling the use of optical diagnostic tools for observation and investigation of the interaction [11].

This phenomenological description demonstrates the difficulty to obtain detailed quantitative information about the interaction. The above-mentioned processes span and may occasionally overlap over multi-decade spatial and temporal intervals. Optical experiments are often used for the investigation of these processes but they are limited intrinsically in terms of spatial (diffraction limit) and temporal resolution (pulse duration). Moreover, almost any modification of the electronic and lattice subsystems results in a change of its optical response making difficult to discern between individual mechanisms occurring simultaneously. To solve these issues, well-engineered experimental techniques must be employed to extract usable quantitative information. In parallel, numerical simulations based on modeling are used in conjunction with experiments to provide information on the hindered parts of the interaction. A validated model would be the corner stone of a digital twin that would allow prediction of the interaction outcome and revolutionize laser-based manufacturing.

The pump-probe technique has been used successfully in transparent solids to capture the ultrafast electron dynamics with femtosecond temporal resolution. Spatially-resolved information may be obtained by combining a pump-probe scheme with microscopy tools. In this context, time-resolved pump-probe shadowgraphy techniques have emerged as a solution for investigating fundamental questions in laser-matter interaction [12]. Several reports discussed transient photoinduced plasma inside the bulk of SiO_2 using either optical transmission measurements [13,14], holography [15] or phase-contrast imaging [16,17]. Other studies explored the relaxation of the laser deposited energy in terms of stress wave emission by the transient-lens method [18] or by polariscopic techniques [19]. In particular, important efforts were made to capture a continuum of experimental observations assessing both the laser energy deposition and material relaxation by Mermillod-Blondin *et al.* [20] and Hayasaki *et al.* [21].

Although many studies exist within a broad timescale, very few provide datasets with quantitative information on the evolution of the thermodynamic state of a material following irradiation by a femtosecond laser pulse exist. Recently, Nguyen et al. [22] provided quantitative measurements in the ns-µs timescale probing the thermomechanical relaxation of crystalline SiO_2 following irradiation by a femtosecond laser Bessel beam. In this study, we aim at bridging this gap by providing quantitative information on the interaction of an intense femtosecond laser gaussian pulse with amorphous SiO_2 on a timescale ranging from few hundreds femtoseconds to several nanoseconds. This achievement allows us to uncover the time evolution of the physical quantities defining the thermodynamic state of the material upon laser processing with high precision from its initial laser excitation to its final transformation. By focusing a near-infrared 360-fs laser pulse inside the bulk of fused silica, we first achieve above-damage optical intensities, corresponding to ~10^{14} W/cm^2 in air. Different optical techniques are then combined to provide a continuum of direct experimental information in a large spatio-temporal domain. We perform time- and space-resolved optical transmission and birefringence measurements of the laser-excited material from the femtosecond to the nanosecond timescales in perpendicular geometry. By use of the Drude-Lorentz and photoelastic models, we deduce the laser-induced carrier density and stress amplitude, respectively. In parallel, we have developed a predictive model, accounting for the electron dynamics, laser propagation and the hydrodynamic relaxation. The model has been experimentally validated and then used to address long-standing unanswered questions. These include for instance the transient pressure-temperature-density evolution of the irradiated material and the relative importance of the different energy relaxation channels, i.e. how the absorbed laser energy is transformed and dissipated into other kinds of energy in the material.

II. Experiment

A. Experimental setup

Figure 1 presents the time-resolved microscope-polariscope setup. A diode-pumped linearly-polarized Yb-doped fiber laser (Satsuma, Amplitude Laser) delivers 20-µJ pulses with 360-fs duration (measured at full width half maximum (FWHM)) and a central wavelength (λ) of 1030 nm. The laser beam is divided in two parts by use of a plate beamsplitter (20% reflection, 80% transmission). The energy of the transmitted (pump) beam is varied by using a half-wave plate and a polarizing beamsplitter cube. Finally, the beam is focused with an aberration-corrected microscope objective (LCPLN50XIR, Olympus) of 0.65 numerical aperture (NA) inside the bulk of a fused silica sample. The sample is mounted on a three-axis motorized translation stage to allow precise positioning. The energy

of the beam is set to 1 μJ after the microscope objective lens by using a calibrated power meter yielding a corresponding calculated peak focused intensity in air of ~ 10^{14} W/cm² (waist w_0 ~ 1 μm).

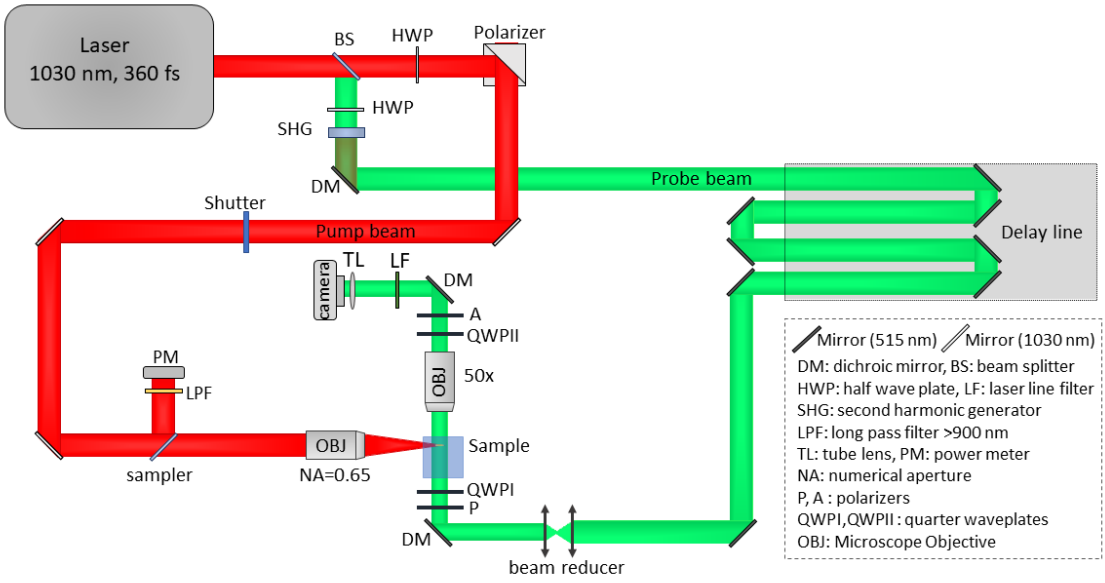

Figure 1. Experimental setup.

The reflected beam on the plate beamsplitter is converted to its second harmonic (λ=515 nm) with the help of a type I beta-barium borate crystal. It is subsequently used for the illumination of the pump-irradiated volume (probe beam) in a Köhler-type perpendicular configuration. This choice enables the estimation of the optical integration length from direct experimental evidence. The pump-irradiated volume is then imaged by means of an objective lens (50x Mitutoyo Plan Apo NIR infinity corrected, NA=0.42) and a CMOS camera (CS165MU Zelux, 3.45 µm square pixel size). The delay of the probe beam with respect to the pump is adjusted by changing the optical path of the probe with a motorized delay line, which is composed of four mirrors, within a range of about 5.5 ns. To acquire dynamic information over the whole range, single-shot irradiation is repeated each time with a different pump-probe delay and always on a fresh site of the sample at the same focusing depth. In overall, this configuration enables femtosecond temporal resolution (supposed to be equal to the probe pulse duration) and micrometric spatial resolution (0.6 µm according to the Abbe diffraction limit).

Birefringence measurements, being only sensitive to anisotropic changes, allow for reliable measurement of stress-induced modifications. Furthermore, the perpendicular configuration between the pump and probe pulses allow the measurement of the integration length, a crucial parameter in quantitatively determining stress-inducing birefringence. To perform birefringence measurements, a circular polariscope is implemented. The probe beam is first circularly polarized before the sample (polarizer P and quarter-waveplate QWPI in Figure 1). It is analyzed after the sample using an elliptical analyzer consisting of a second quarter-waveplate (QWPII) and a polarizer (A) mounted on separate motorized rotation stages. Phase-shifting techniques can be used to retrieve the retardance of the sample [23]. We employ the Hecker and Morche arrangement [24], which yields a satisfactory compromise between accuracy and acquisition speed. To obtain a retardance map, five images are recorded with different analyzer settings corresponding to different orientations for QWPII and A. In between recordings, the sample is spatially shifted to always impinge on a pristine SiO_2 volume. One of the settings corresponds to the brightfield arrangement. It is simply the transmitted probe intensity in the absence of any analyzer. By dividing the transmitted probe intensity with and without the pump beam, we obtain the optical transmission. Finally, the signal-to-noise ratio is improved by systematically correcting for the background retardance of the sample and averaging over images. The accuracy of our setup has been calibrated by employing a variable Soleil-Babinet retarder.

B. Experimental results

The laser is operated in single-shot mode and the pump pulse is focused at a depth of 600 µm inside a polished SiO_2 cube (Heraeus Spectrosil2000). Pulse elongation due to chromatic dispersion is negligible due to low group velocity dispersion in SiO_2 at the pump wavelength. The intensity is maintained constant for all experiments and corresponding to a calculated peak optical intensity (in air) of ~10^{14} W/cm^2. Using the above-mentioned pump-and-probe microscope-polariscope we record the isotropic (transmission) and anisotropic (birefringence) optical response of the sample upon laser irradiation. Time-resolved optical transmission and retardance measurements are presented in Figure 2. In all of these images, the pump pulse is propagating from right to left (wavevector k_{pump}) while the probe pulse is propagating perpendicular to the screen towards the observer (wavector k_{probe}).

The zero-time delay has been arbitrarily chosen as the beginning of the transmission drop due to the arrival of the pump pulse. Focusing on the transmission measurements at short delays (Figure 2a), we observe a swift drop in the transmission at 200-fs time delay. This drop is attributed to free carrier absorption previously generated by the pump beam due to photoionization. At this stage, we note that transmission measurements are sensitive on both attenuation and diffraction of the probe beam. When a phase object is created (Figure 2a), diffraction generates a wavy modulation of the transmission. The transmission reaches its minimum approximately 600 fs after zero-time delay. Starting at 800 fs, we observe the rise of the transmission level again locally indicating that the free-electron population begins to decrease in the focal volume with complete recombination occurring for nanosecond delays. At around 10 ps, a white spot appears locally at approximately the time where the transmission has been minimum before (0.6 ps delay) indicating that transmission dynamics varies across the trace following variation of the deposited energy density. Transmission measurements within our conditions are affected by changes in both real and imaginary parts of the refractive index making it difficult to discern between different contributions including the temperature rise. At ~1 ns, we have slightly modified the distance between the plasma and the imaging objective in order to better visualize the stress wave in transmission. This results in the sudden change of transmission measurement. After two nanoseconds from the arrival of the pump pulse we observe the formation and propagation of a stress wave that can be identified by the local change in the transmission (Figure 2b). *Post mortem* transmission measurement on the irradiated sites (Figure 2e) reveals a permanent modification of the material, demonstrating the use of an above-damage threshold intensity in the experiment.

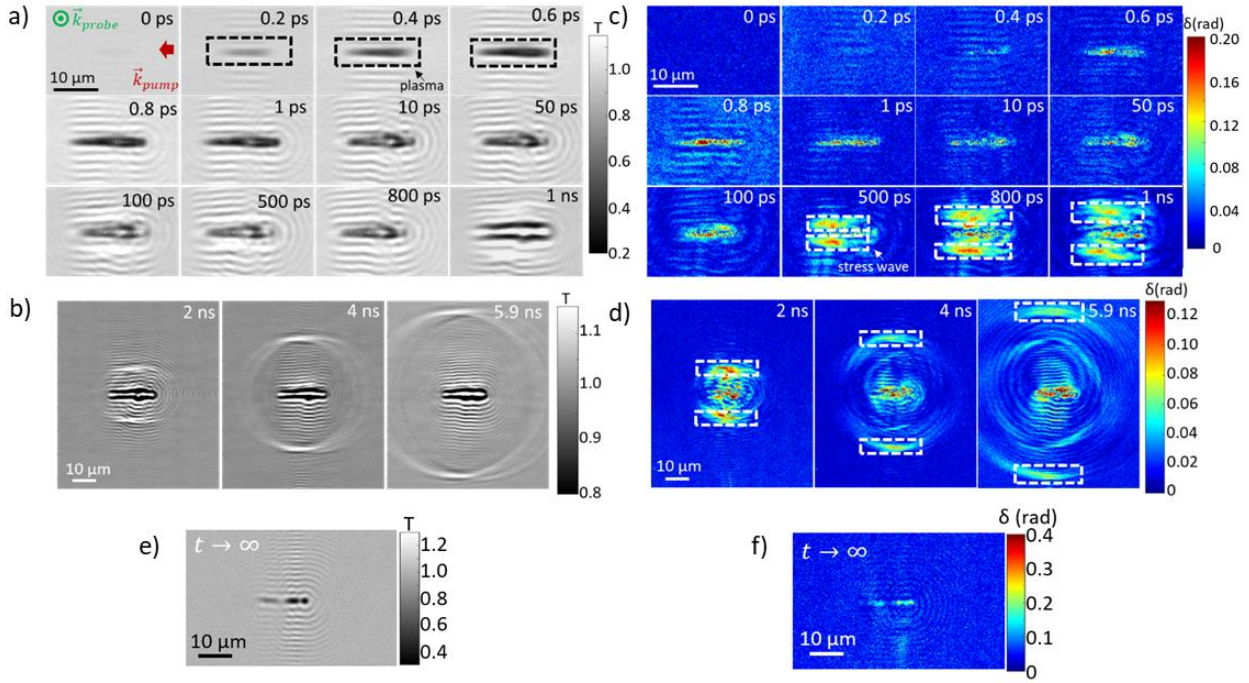

Figure 2. Dynamic observation of the optical transmission (a,b,e) and retardance (c,d) modifications induced by a 1-µJ laser pulse inside SiO_2. A free-carrier plasma is formed during the first hundreds of femtoseconds (a) followed by stress wave generation and propagation (c,d) before an irreversible modification is observed at the end of the interaction (e,f).

We obtain complementary results about the interaction by measuring the optical retardance. In Figure 2c, we present retardance maps for pump-probe delays from zero to one nanosecond. An increase of the birefringence signal is observed at around 400 fs inside the focal volume. Being more accurate than the transmission images to capture such information, the stress wave emission is detected earlier at 500-ps time delay and its outward propagation perpendicular to the optical axis is recorded until 6 ns. At late delays (Figure 2d), this stress wave is propagating at a measured speed equal to the acoustic velocity of the material, approximately 5.72 µm/ns [25]. Experimental artefacts and limited spatial resolution hinder the determination of the exact shockwave position for short delays (<1ns), therefore not excluding the presence of shockwave propagation at these delays. The optical retardance decays from 120 mrad to approximately 50 mrad within this timeframe revealing the decaying amplitude of the stress wave. Retardance measurements of the final modified structure reveals stress presence as illustrated in Figure 2f. A more detailed discussion on the precise nature of this wave will follow in section IV.

III. Multiscale modeling

As mentioned in the introduction of this paper, a multiscale model describing the interaction of a femtosecond laser pulse with a dielectric material should include, first, the coupled microscopic electron dynamics and laser propagation, and, second, the macroscopic hydrodynamic material response. Before presenting each part in detail, the synopsis and main assumptions of our multiscale modeling is briefly presented. First the laser energy deposition is determined by describing the coupled laser propagation and electron dynamics. The laser propagation is described by the nonlinear Schrödinger equation within the framework of the paraxial assumption. The laser reflection is thus neglected; the Kerr effect is also not included. The optical material response is evaluated with the standard Drude model which depends in particular on the free electron density. The latter is evaluated with a rate equation which accounts for photoionization, impact ionization, and electron recombination. Previous calculations provide the distribution in space of the energy density of free electrons just after the laser irradiation. Assuming this energy density is transferred into the lattice on a timescale much shorter than the material hydrodynamic response, the equivalent internal energy brought by the laser is used as an initial condition to carry out hydrodynamic simulations which also include the mechanical material response. Since hydrodynamics take place when there is no longer laser irradiation, a single temperature is assumed. Also, a one-dimensional cylindrical geometry is considered which is close to experimental observations.

In our operating conditions using 360-fs near-IR single laser pulse, the laser-induced electron dynamics is described with the standard rate equation providing the evolution of the free electron density, which has been shown to correctly account for various experimental observations [26]. In addition, such an approach is not computationally expensive (compared with *ab initio* calculations for instance), allowing us to build a numerically efficient multiscale-multiphysics model well adapted for parametric studies. Within the present framework, the rate equation providing the evolution of the free electron density, n_e, reads:

$$\frac{dn_e}{dt} = \left(1 - \frac{n_e}{n_a}\right)\left(W_{PI} + \frac{\sigma_{col} I}{E_g} n_e\right) - \frac{n_e}{\tau_r} \tag{1}$$

Where W_{PI} is the photo-ionization rate reading $\sigma_8 I^8$ with σ_8 the generalized eight-photon absorption cross section to bridge the bandgap (value provided later). I is the laser intensity, E_g the material bandgap is set to 9 eV [27], τ_r the self-trapped exciton recombination time that should be accounted for in fused silica is set to 150 fs [28], and n_a the density of valence electrons that could be ionized, is set to 2 10^{22} cm^{-3} [29]. The term $(1-n_e/n_a)$ accounts for the depletion of the valence band. The absorption cross section, σ_{col}, obtained with the Drude model reads:

$$\sigma_{col} = \frac{e^2 \nu_c}{\varepsilon_0 n_0 c m_e (\omega^2 + \nu_c^2)} \tag{2}$$

Where ε_0 is the vacuum dielectric permittivity, e and m_e the electron charge and mass, respectively, n_0 the material refractive index set to *1.45*, c the speed of light, ω the laser frequency, and ν_c the electron collision frequency (value provided later). This description of the laser-induced free electron dynamics involves the following assumptions to build a computationally efficient multiscale approach. The contribution of self-trapped excitons to the ionization is not included and only multiphoton absorption is considered (no tunneling). Since there is an adjustable parameter for the photo-ionization process (σ_8), it can account implicitly for all processes. It is worth noting that despite the nonlinear behavior of the process, we have observed a rather low sensitivity of simulation results with respect to this

parameter due to a self-saturation mechanism (discussed in section IV). This implies a low sensitivity on the precise nature of the ionization process. The electron transport is also neglected as usually done for dielectrics within the present physical conditions [30].

Experimental results shown in Figure 2 demonstrate an elongated absorption area around the focal plane position, of length similar to the confocal length (calculated to be ~9 µm). This area appears rather homogeneous (see figure 2a) indicating that the absorption of laser energy develops in a large volume following beam propagation with negligible contribution from nonlinear propagation effects (not detected in our experiments). This smooth propagation of the laser beam is also supported by the use of i) a small peak power in comparison with the critical power ($P_{peak}/P_{critical}=0.56 < 1$), ii) a high focusing NA objective (limiting the length over which the nonlinear phase effects can develop) and iii) the self-saturation intensity effect [31] that limits the intensity delivered in the bulk of a dielectric. We thus further assume that the spatio-temporal structure of the Gaussian laser beam is nearly unchanged in the course of interaction, which is in line with a free electron density lower or close to the critical plasma density [32,33]. Under these conditions, the laser light reflection also remains low. The mechanical information further shows a moderate amplitude of stress waves (with moderate material damage), also suggesting a moderate laser energy deposition into the material. Within the scope of building a numerically efficient multiscale-multiphysics model, the previous conclusion from experimental observations leads us to model the laser propagation within the paraxial approximation instead of solving Maxwell equations. It is important to note that despite the moderate NA (0.65) used for the pump beam, refraction inside SiO_2 significantly lowers the vacuum equivalent NA down to ~0.45. This is smaller than the NA values leading to considerable nonparaxial and vectorial effects during the propagation [34]. This assumption will be also validated *a posteriori*. The axi-symmetric equation driving the evolution of the laser electric field, *E*, then reads [26,32]:

$$\frac{\partial E}{\partial z} = \left(\frac{i}{2k_0}\Delta_r - \frac{\sigma_{col}}{2}n_e - \frac{W_{pi}E_g}{2I}\right)E \tag{3}$$

Where *z* and *r* are the longitudinal (direction of laser propagation) and radial coordinates, respectively. Δ_r accounts for the diffraction within the cylindrical symmetry. The following terms are consistent with Eq. (1) and lead to both intensity attenuation in course of propagation and energy deposition into the material.

Figure 3 illustrates the coupled dynamics of electron population and laser field. Considering interaction in vacuum (without any excited material), Figure 3a shows that the laser intensity distribution in space is symmetric as expected, accounting for the free propagation of a Gaussian field. The coupling with the electron dynamics generated in the excited material breaks this symmetry as depicted by Figure 3b which shows the distribution of absorbed laser energy density in space after the interaction. As already described in [26,33], the first part of the propagation in front of the focal point has a Gaussian shape following the laser beam distribution. This is consistent with the low intensity ahead of the focal point inducing a weak absorption and a small number of free electrons. High intensity is reached nearly at the focal point yielding strong absorption and a large population of free electrons. This further leads to a significant decrease in the laser intensity, which then is not able to further ionize the material beyond the focal point, leading to the observed asymmetry.

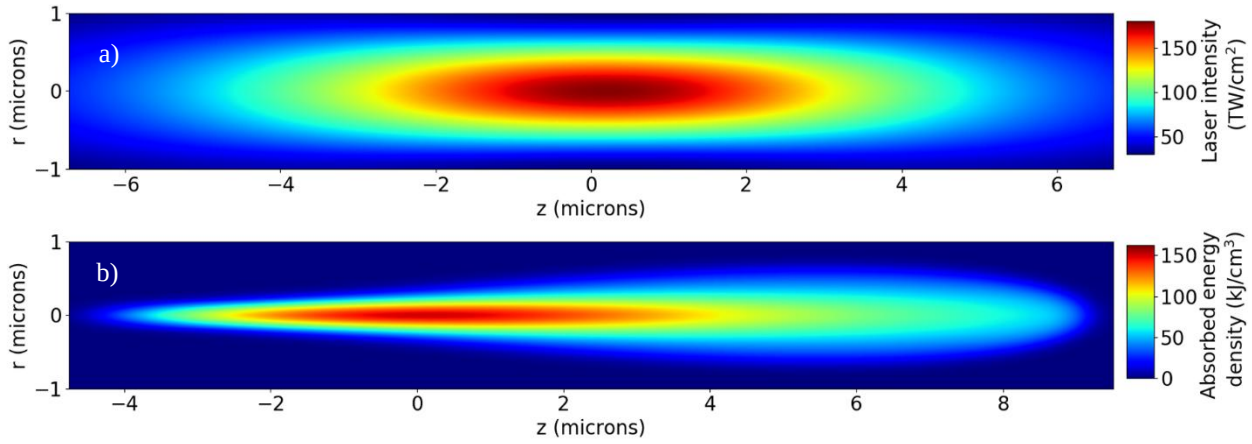

Figure 3. (a) Intensity profile without interaction, it is symmetric with respect to the propagation direction z. (b) Spatial profile of absorbed energy density in the material as predicted by the present model, the symmetry is broken (see text). Note that the horizontal axes are slightly different to exhibit the change in symmetry. The laser pulse is propagating from right to left towards negative z.

Because the characteristic timescales of energy deposition and hydrodynamics are significantly different (a few hundred fs and a few tens of ps, respectively), the energy deposition previously evaluated from the electron dynamics and beam propagation modelling is used as an initial source term for the hydrodynamics simulations. Those processes and simulations developing at a later time scale (>> 1 ps), electron-lattice relaxation is assumed to be finished and thermal equilibrium is reached. Therefore, no Two-Temperature model is used in our approach and in the corresponding equations only a single temperature is considered. Further, cylindrical symmetry is considered because the initial energy deposition has a large enough aspect ratio (elongated in the direction of laser propagation as observed experimentally). Finally, these simulations are carried out in the radial direction with the Esther code which solves Euler equations (hydrodynamics) including mechanical material behavior (deviatoric component of stress) and heat diffusion [35]. Sesame table 7387 defining the equation of state (EOS) of fused silica including the various states of matter is used and the mechanical behavior is assumed to be elasto-plastic [36,37]. The elastic limit and the shear modulus are set to 7.1 GPa and 22.6 GPa, respectively. Both tend smoothly to zero at the softening point set to 2.15 kJ/g.

The coupled equations (1) and (3) are numerically solved with a finite difference scheme. Note that both excited electron density and laser electric field depend on space and time. The electron density is initially set to zero everywhere, and the laser electric field is propagated from a Gaussian field as boundary condition (with a waist of *1 µm* at the focal point). We have checked that the numerical convergence is achieved in terms of space and time discretization and domain size. The obtained 2D energy deposition is averaged over the direction of laser propagation to provide the initial condition of hydrodynamic simulations, i.e. a radial profile of internal energy.
Considering widely used value of photoionization cross section (order of magnitude of empirical expression of Agostini and Petite [38]) and inverse of collision frequency in the standard femtosecond range ($1/\nu_c$ = 3.7 fs for critical plasma [39]), we correctly reproduce the magnitude of absorption and amplitude of stress waves in the GPa range. More precisely, the microscopic modeling parameters have been set to precisely account for the experimentally measured maximum stress amplitude at t = 1 ns which is close to 1 GPa, determining: $\sigma_8 = 10^{-270}$ $m^{16}s^{-7}$ and ν_c^{-1} = 4 fs.

Simulations of the macroscopic material response can then be performed. Figure 4 shows the obtained spatial profile of principal stress difference $\Delta\sigma = \sigma_r - \sigma_z$ with σ_r, σ_z the principal stresses in cylindrical coordinates for suitable comparison to the experimental observation. The stress wave can be clearly observed in a nanosecond timescale consistent with experimental observations (after 500 ps, two symmetric structures appear). Profiles for a sub-nanosecond timescale are provided in section IV. The propagation of a stress wave clearly appears. The positions of the wave are in a good agreement with experimental observations, with a velocity of ~5.5 µm/ns which corresponds to the sound speed, c_s. The compression wave (positive stress) is followed by a rarefaction wave (negative stress) which originates from the very early stress relaxation associated with the formation of a cavity in the interaction

region [36,37]. The final important characteristic of this dynamics is the attenuation of the wave in the course of propagation, decreasing from 1.5 GPa to 0.25 GPa at the end of the observation, i.e. by a factor of 6. The processes at play are discussed in section IV.

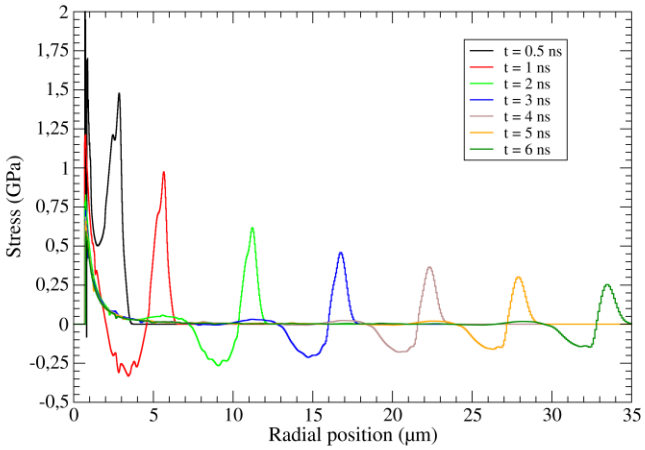

Figure 4. Theoretical spatial evolution of the stress at various times. The wave propagation can be observed. The initial time corresponds to the end of the laser energy deposition into the material.

IV. Analysis and Discussion

First, we compare the experimental results with simulations in order to validate our model in a large temporal interval. From the probe transmission results of Figure 3a, it is possible to calculate the average absorption coefficient $a = (2\omega/c) \times \mathrm{Im}(n)$ at the center of the energy deposition volume, with n the refractive index of the excited material. We consider that the free carriers are homogeneously distributed in a cylinder. Then, to calculate the transmission perpendicular to the long axis of the cylinder we simply use the Beer-Lambert Law neglecting reflectivity:

$$T = e^{-a \cdot l} \tag{4}$$

With l the traveled distance inside the cylinder equal to its diameter. At *600 fs*, we extract the minimum transmission level at around 30%. The diameter of the cylinder can be estimated from a vertical transmission profile (perpendicular to the pump pulse propagation axis). Taken as equal to the FWHM, we measure 1.6 µm. Finally, using the Drude-Lorentz model (see section III), we calculate the carrier density n_e=3.80 10^{21} cm^{-3}. This value is approximately equal to 3.6 times the critical density at the pump wavelength n_{critical}=1.05 10^{21} cm^{-3}, demonstrating the generation of a highly-absorbing, slightly overcritical plasma, consistent with the observed permanent damage of the material.

Numerical simulations presented in Figure 3 confirm the previous analysis. By averaging in time and space, we obtain an electron density of the same order of magnitude. It is worth mentioning that the paraxial approximation used to model the laser propagation is not strictly valid within such a condition but forms an acceptable approximation. As a demonstration, we recall that the theoretical shape of absorbed energy is in a very good agreement with the plasma observation (Figure 3b can be compared with Figure 2a since absorption and transmission are mainly proportional to the free electron density). By analyzing numerical results, the laser energy deposition into the material can be evaluated. We obtain roughly 250 nJ. Since the incident laser energy is 1 µJ, that corresponds to a total absorption of 25 %.

On the other hand, birefringence measurements allow estimating the laser-induced stress inside the material. The photo-elastic effect expresses that the dielectric permittivity is a function of stress/strain inside a transparent

material. According to the stress-optic law, the optical retardance δ is linearly connected to the principal stress difference Δσ with the relation $\delta = \frac{2\pi h}{\lambda} C \cdot \Delta\sigma$ [40] where λ is the probe wavelength, h the path length and C the stress-optic coefficient equal to 2.5 10^{-12} $N^{-1}m^2$ for SiO_2 at λ=515 nm [41]. Next, we consider that the shape of the laser-induced stress wave can be modeled by a hollow cylinder surrounding the focal volume with its height along the pump propagation direction. The difference between the outer and inner radii is equal to the optical thickness of the stress wave that can be accessed by plotting a vertical profile along the direction perpendicular to the optical axis of the pump beam (Figure 2d). Then, the path length is equal to twice the chord length that is tangent to the inner circle and can be easily retrieved geometrically. The expansion of the stress wave results in the increase of the path length in between different delays and it has to be accounted for to provide quantitative information about the generated stress. It is important to note that determination of the path length with a precision better than 10% is not possible in our conditions and that precise evaluation of the stress value should involve Abel transform algorithms that are out of the scope of this study. The retrieved principal stress difference as a function of the pump-probe delay is plotted in Figure 5. The generated stress level is measured in the GPa range for sub-nanosecond delays (0.5-1 ns) before dropping down to the 100-MPa range at later delays (1-6 ns). At all times, the generated stress wave is measured to propagate at the speed of sound. This is in contrast with laser-induced shockwaves observed in air [42] or at the interface between SiO_2 surface and air [43] where supersonic conditions are reached.

Modelling results in section III indicate that the hydrodynamics proceeds in the acoustic regime within the present laser irradiation conditions for delays longer than roughly 500 ps. The maximum stress with respect to time can be extracted from these results. It is reported in Figure 5 and directly compared with the experimental observation. There is a good general agreement over the whole considered timescale. Since the stress wave evolves within the acoustic regime, no attenuation is expected (for shocks, the attenuation is mainly due to the rarefaction wave which meets the shock front). Visco-thermal damping should also not contribute on this timescale [44]. The attenuation then is attributed to the spreading of acoustic wave energy in space. Within a cylindrical symmetry and propagation along the radial coordinate, the amplitude is expected to evolve as $1/r$. With $r(t) = r_0 + c_s.t$, a good fit of the maximum stress evolution is obtained (result not shown), confirming the geometrical attenuation. The possible main difference between experimental and theoretical results appears for longest delays above 3-4 ns. For long delays, the wave propagation no longer obeys the theoretical cylindrical symmetry because its radial position is of the same order of magnitude as the length (along z) of the absorbing area, of the order of 15 µm. The wave amplitude thus should decrease faster in this region, and as $1/r^2$ asymptotically (spherical expansion with a point source). That explains why modeling predicts larger amplitudes in this region.

Post-mortem analysis indicates that within the observed discontinuous damage track (Figure 2e), a dark scattering point appears, next a region with no transmission change and again a region with lowered transmission. Similar morphologies have been observed by other authors [45,46] where dark points correlate with low-density regions revealed by phase contrast microscopy. Formation of void-like structures has been the subject of several investigations, with their formation being attributed on either ultrafast formation from rarefaction wave following microexplosion [47] or a much slower process in the presence of a phase transition where viscosity is considerably lowered allowing cavity formation [48]. Furthermore, internal transformations towards densified structures have been already demonstrated [49].

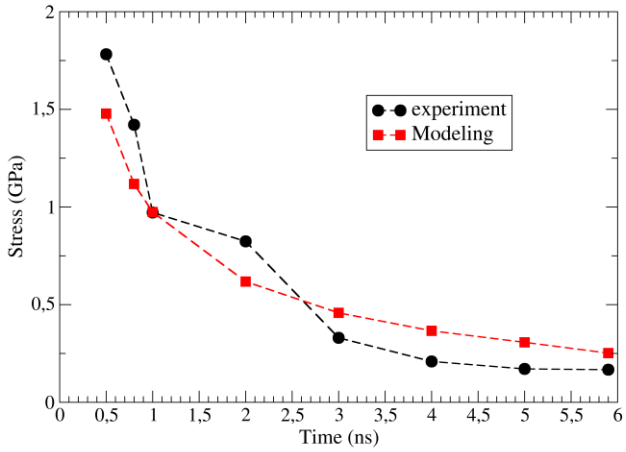

Figure 5. Principal stress difference as a function of pump-probe delay. Experimental (black dashed line) and simulation (red dashed line) are shown. The decrease in the amplitude is due to geometric attenuation (see text).

The modeling is also expected to provide reliable information on physical quantities and processes in regions currently not accessible by our experiment, in particular how the absorbed laser energy transforms into other forms including mechanical deformations and hydrodynamics constraints on a sub-nanosecond timescale. Figure 6 provides such physical information, where is shown the evolution of stress, material density and temperature as predicted by the present modeling. After the laser energy deposition and before hydrodynamic relaxation, Figure 6a shows that the maximum stress is in excess of 20 GPa on central axis of laser propagation (*r=0*), i.e. more than one order of magnitude larger than the value observed at 500 ps. Discussing the calculated pressure of 20 GPa is essentially equivalent to discussing the calculated deposited energy density of approximately 150 kJ/cm^3 (refer to Figure 3b) as both are connected by the EOS. It is therefore important to highlight that this calculated energy accurately replicates the experimental stress measurements (see Figure 5). While considering the potential experimental errors and the assumptions inherent in our model, an overestimation of this value cannot be ruled out, although its order of magnitude aligns with the expected physical processes. Specifically, this value is anticipated to be significantly greater than the melting enthalpy of fused silica (~5 kJ/cm^3) as indicated by the notable hydrodynamic response evidenced by the visualization of intense stress waves (see Figure 2). Similar energy densities in the range of a few hundred of kJ/cm^3, with peak values around 300 kJ/cm^3, have recently been reported by Rudenko et al. [50].

A strong and fast decrease in the pressure is observed in Figure 6a and it is due to the formation of a cavity on a timescale of 100 ps as shown by Figure 6b where the material density drops down to 0.2 g/cm^3 (initial density is 2.2 g/cm^3). The near-void formation is due to the central pressure which expels matter [36,47]. The pressure first drops because it is nearly proportional to the density (EOS) and because of energy transformation to kinetic energy: numerical simulations indicate that matter is expelled with a velocity in excess of hundreds of m/s. Between 100 ps and 200 ps, the pressure profiles of Figure 6a show that the short scale hydrodynamic relaxation stops, and gives rise to the formation of a stress wave that can escape from the interaction region. Indeed, this timescale is the ratio between the size of the region in with significant laser energy deposition occurs, and the speed of sound, i.e. ~ 1 µm / 5.5 µm/ns = 180 ps. The first instant where the stress wave can be clearly distinguished is indeed around 180 ps as shown by Figure 6a, in which the associated maximum stress is depicted by the vertical arrow. This delay is very similar to the one experimentally retrieved of few hundreds of picoseconds (Figure 2c). It is interesting to evaluate whether an electronic contribution can be the main mechanism behind this pressure wave emission. However, in that case the wave would have been detected at earlier delays (~500 fs) when carrier density is at its maximum value. Furthermore, estimating the electronic pressure as $P_e=n_e k_b T_e$ with k_b the Boltzmann constant and T_e the average electronic temperature set to 5 eV, we obtain P_e~800 MPa which is negligible compared to the matrix pressure of ~20 GPa obtained from our model. Therefore, we attribute the origin of this wave to the matrix response following the laser energy deposition.

Figure 4 shows the propagation of this wave on a longer timescale. After a delay time of 2 ns (see Figure 6b), the cavity closes because not enough energy was absorbed [36]. The origin of kinetic energy is first due to the

matter movement associated with cavity formation and then is due to the stress wave. By analyzing numerical results, it appears that the kinetic energy associated with the cavity dynamics and the stress wave energy are rather similar, close to 5 nJ. Since the energy deposition is around 250 nJ, 2 % of the absorbed laser energy is transformed into mechanical energy. The rest, 98 %, is transformed into heat, with a maximum material temperature of about 35000 K. Once again, the calculated temperature is linked to the calculated energy density of approximately 150 kJ/cm^3 via the EOS.

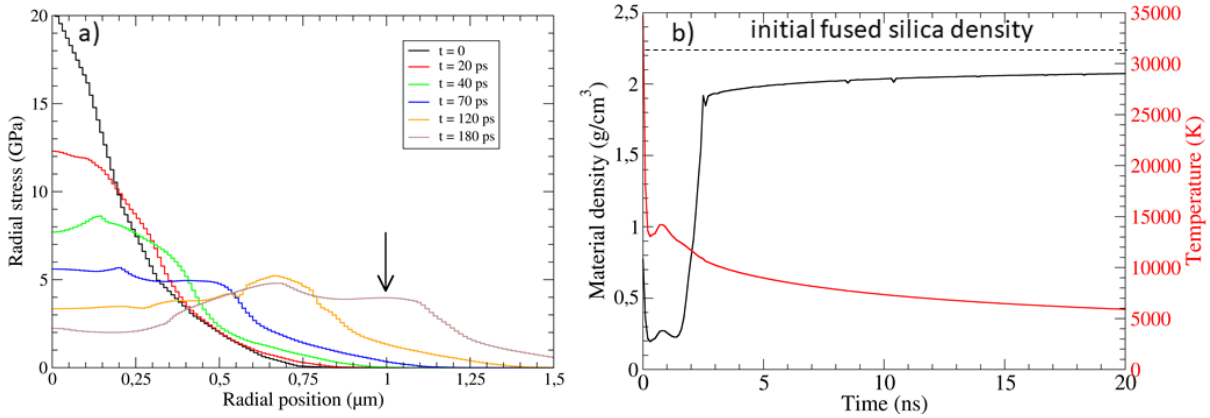

Figure 6. Numerical simulations to exhibit physical processes on the short sub-nanosecond timescale. (a) Spatial profile of stress. The vertical arrow shows the position of the launched stress wave when it can be clearly distinguished from the stress background. (b) Both material density and temperature as a function of time on central axis of laser propagation (r = 0).

After 2 ns a long scale hydrodynamic relaxation takes place in the interaction region as shown by Figure 6b. The material density goes back to 2 g/cm^3, i.e. not the initial density within these timescales. In the same time, the temperature drops due to diffusion and resolidification.

We finish this discussion on the possible formation of a laser-induced shock wave. When numerically measuring the speed of the wave after a few ns, we obtain ~ 5.5 µm/ns which corresponds to the sound speed. Here the wave pertains to an acoustic wave. When measuring its speed right when it is launched from the interaction area (at t = 200 ps), we obtain 5.89 µm/ns, i.e. slightly faster than the sound speed. This suggests the formation of a weak shock wave, which is consistent with a pressure of a few GPa corresponding to the upper limit of the acoustic regime. After a few microns of propagation, the pressure amplitude decreases, and the initial shock wave transforms into an acoustic wave.

V. Conclusions

In conclusion, we have investigated the interaction of a femtosecond laser pulse with SiO_2 from the early photoionization stage and energy deposition until its dissipation by means of stress wave emission. Our results bridge various physical processes taking place on different temporal and spatial scales. By focusing an infrared (1.03 µm) femtosecond (360 fs) laser pulse at above damage threshold intensity inside the bulk of SiO_2, we have generated an absorbing micrometric plasma. Time-resolved transmission microscopy was used to measure a maximum carrier density slightly in excess of the critical plasma density. Simultaneous time-resolved birefringence microscopy was used to directly measure ~GPa stress induced by the acoustic wave passage inside the material. A multiscale model with only two free microscopic parameters was developed to account for the laser pulse propagation, electron dynamics and the macroscopic hydrodynamic response of the material. Following experimental validation, simulations provided additional insights into the interaction. Our numerical simulations suggest that the laser-irradiated volume is loaded with a maximum stress of 20 GPa and a temperature of 3.5 10^4 K. To obtain these results, we rely on the validation of the numerical simulations with experimental measurements therefore being potentially sensitive to experimental artifacts discussed in section II.B. A weak shockwave is emitted at around 200 ps that quickly degenerates into the experimentally observed acoustic wave. Terapascal generated pressures have been reported before to explain the formation of cavities by microexplosion [47]. However, recent theoretical investigations demonstrate that intensity clamping results in the achievement of more modest stress increases in the hundred GPa range [50]. Our approach could contribute to experimentally verifying such assertions

in the future. Only 2% of the absorbed laser energy is transformed into a shockwave while the remaining energy is dissipated following a thermal pathway. In the future, our methodology can be used for further parametric studies such as laser pulse energy and number of pulses, providing a descriptive and reliable prediction tool for laser-based material processing.

VI. Bibliography

1. K. Sugioka and Y. Cheng, "Ultrafast lasers-reliable tools for advanced materials processing," Light Sci. Appl. **3**(390), e149 (2014).
2. M. Malinauskas, A. Žukauskas, S. Hasegawa, Y. Hayasaki, V. Mizeikis, R. Buividas, and S. Juodkazis, "Ultrafast laser processing of materials: From science to industry," Light Sci. Appl. **5**(8), 3–5 (2016).
3. R. Osellame, G. Cerullo, and R. Ramponi, "Femtosecond Laser Micromachining: Photonic and Microfluidic Devices in Transparent Materials," Top. Appl. Phys. **123**, 3–19 (2012).
4. J. Zhang, M. Gecevičius, M. Beresna, and P. G. Kazansky, "Seemingly unlimited lifetime data storage in nanostructured glass," Phys. Rev. Lett. **112**(3), 033901 (2014).
5. F. Sima, K. Sugioka, R. M. Vázquez, R. Osellame, L. Kelemen, and P. Ormos, "Three-dimensional femtosecond laser processing for lab-on-a-chip applications," Nanophotonics **7**(3), 1–22 (2018).
6. A. Vailionis, E. G. Gamaly, V. Mizeikis, W. Yang, A. V. Rode, and S. Juodkazis, "Evidence of superdense aluminium synthesized by ultrafast microexplosion," Nat. Commun. **2**, 445 (2011).
7. S. Han, L. Ortmann, H. Kim, Y. W. Kim, T. Oka, A. Chacon, B. Doran, M. Ciappina, M. Lewenstein, S. W. Kim, S. Kim, and A. S. Landsman, "Extraction of higher-order nonlinear electronic response in solids using high harmonic generation," Nat. Commun. **10**(1), 1–6 (2019).
8. T. Winkler, L. Haahr-Lillevang, C. Sarpe, B. Zielinski, N. Götte, A. Senftleben, P. Balling, and T. Baumert, "Laser amplification in excited dielectrics," Nat. Phys. **14**(1), 74–79 (2018).
9. E. G. Gamaly and a. V. Rode, "Physics of ultra-short laser interaction with matter: From phonon excitation to ultimate transformations," Prog. Quantum Electron. **37**(5), 215–323 (2013).
10. N. M. Bulgakova, V. P. Zhukov, S. V. Sonina, and Y. P. Meshcheryakov, "Modification of transparent materials with ultrashort laser pulses: What is energetically and mechanically meaningful?," J. Appl. Phys. **118**(23), (2015).
11. E. G. Gamaly and A. V. Rode, "Transient optical properties of dielectrics and semiconductors excited by an ultrashort laser pulse," J. Opt. Soc. Am. B **31**(11), C36 (2014).
12. B. Guo, J. Sun, Y. F. Lu, and L. Jiang, "Ultrafast dynamics observation during femtosecond laser-material interaction," Int. J. Extrem. Manuf. **1**(3), (2019).
13. C. Pan, L. Jiang, Q. Wang, J. Sun, G. Wang, and Y. Lu, "Temporal-spatial measurement of electron relaxation time in femtosecond laser induced plasma using two-color pump-probe imaging technique," Appl. Phys. Lett. **112**(19), (2018).
14. K. Bergner, B. Seyfarth, K. A. Lammers, T. Ullsperger, S. Döring, M. Heinrich, M. Kumkar, D. Flamm, A. Tünnermann, and S. Nolte, "Spatio-temporal analysis of glass volume processing using ultrashort laser pulses," Appl. Opt. **57**(16), 4618 (2018).
15. D. G. Papazoglou and S. Tzortzakis, "In-line holography for the characterization of ultrafast laser filamentation in transparent media," Appl. Phys. Lett. **93**(4), 93–95 (2008).
16. A. Mermillod-Blondin, C. Mauclair, J. Bonse, R. Stoian, E. Audouard, A. Rosenfeld, and I. V Hertel, "Time-resolved imaging of laser-induced refractive index changes in transparent media," Rev. Sci. Instrum. **82**(3), 033703 (2011).
17. J. Bonse, T. Seuthe, M. Grehn, M. Eberstein, A. Rosenfeld, and A. Mermillod-Blondin, "Time‐resolved microscopy of fs‐laser‐induced heat flows in glasses," Appl. Phys. A Mater. Sci. Process. **124**, 1–6 (2018).
18. M. Sakakura, M. Terazima, Y. Shimotsuma, K. Miura, and K. Hirao, "Observation of pressure wave generated by focusing a femtosecond laser pulse inside a glass," Opt. Express **15**(9), 5674 (2007).
19. M. Sakakura, Y. Shimotsuma, and K. Miura, "Observation of stress wave and thermal stress in ultrashort pulse laser bulk processing inside glass," J. Laser Micro Nanoeng. **12**(2), 159–164 (2017).
20. A. Mermillod-Blondin, C. Mauclair, A. Rosenfeld, J. Bonse, I. V. Hertel, E. Audouard, and R. Stoian, "Size correction in ultrafast laser processing of fused silica by temporal pulse shaping," Appl. Phys. Lett. **93**(2), 1–4 (2008).
21. Y. Hayasaki, M. Isaka, A. Takita, and S. Juodkazis, "Time-resolved interferometry of femtosecond- laser-induced processes under tight focusing and close-to-optical breakdown inside borosilicate glass," Opt.

Express **19**(7), 5725–5734 (2011).
22. H. D. Nguyen, A. Tsaturyan, S. S. Joao, R. Dwivedi, A. Melkonyan, C. D'Amico, E. Kachan, J. P. Colombier, G. Kermouche, and R. Stoian, "Quantitative Mapping of Transient Thermodynamic States in Ultrafast Laser Nanostructuring of Quartz," Ultrafast Sci. **4**, 1–10 (2024).
23. K. Ramesh, T. Kasimayan, and B. Neethi Simon, "Digital photoelasticity - A comprehensive review," J. Strain Anal. Eng. Des. **46**(4), 245–266 (2011).
24. F. W. Hecker and B. Morche, "Computer-Aided Measurement of Relative Retardations in Plane Photoelasticity," in *Experimental Stress Analysis*, H. Wieringa, ed. (Springer, Dordrecht, 1986), pp. 535–542.
25. UQG optics, "Heraeus Spectrosil 2000 data sheet," https://www.uqgoptics.com/wp-content/uploads/2019/03/Heraeus-Spectrosil-2000.pdf.
26. O. D. Caulier, K. Mishchik, B. Chimier, S. Skupin, A. Bourgeade, J. Lopez, V. Tikhonchuk, and G. Duchateau, "Femtosecond laser pulse train interaction with dielectric materials," Appl. Phys. Lett. **107**(181110), (2015).
27. T. H. Distefano and D. E. Eastman, "The band edge of amorphous SiO2 by photoinjection and photoconductivity measurements," Solid State Commun. **9**, 2259–2261 (1971).
28. P. Audebert, P. Daguzan, A. Dos Santos, J. C. Gauthier, J. P. Geindre, S. Guizard, G. Hamoniaux, K. Krastev, P. Martin, G. Petite, and A. Antonetti, "Space-time observation of an electron gas in SiO2," Phys. Rev. Lett. **73**(14), 1990–1993 (1994).
29. A. Q. Wu, I. H. Chowdhury, and X. Xu, "Femtosecond laser absorption in fused silica : Numerical and experimental investigation," Phys. Rev. B **72**(8), 085128 (2005).
30. E. G. Gamaly, "The physics of ultra-short laser interaction with solids at non-relativistic intensities," Phys. Rep. **508**(4–5), 91–243 (2011).
31. D. M. Rayner, A. Naumov, and P. B. Corkum, "Ultrashort pulse non-linear optical absorption in transparent media," Opt. Express **13**(9), 3208 (2005).
32. L. Sudrie, A. Couairon, M. Franco, B. Lamouroux, B. Prade, S. Tzortzakis, and A. Mysyrowicz, "Femtosecond Laser-Induced Damage and Filamentary Propagation in Fused Silica," Phys. Rev. Lett. **89**(18), 186601 (2002).
33. A. Couairon, L. Sudrie, M. Franco, B. Prade, and A. Mysyrowicz, "Filamentation and damage in fused silica induced by tightly focused femtosecond laser pulses," Phys. Rev. B - Condens. Matter Mater. Phys. **71**(12), 125435 (2005).
34. A. Couairon, O. G. Kosareva, N. A. Panov, D. E. Shipilo, V. A. Andreeva, V. Jukna, and F. Nesa, "Propagation equation for tight-focusing by a parabolic mirror," Opt. Express **23**(24), 627–631 (2015).
35. S. Bardy, B. Aubert, T. Bergara, L. Berthe, P. Combis, D. Hébert, E. Lescoute, Y. Rouchausse, and L. Videau, "Development of a numerical code for laser-induced shock waves applications," Opt. Laser Technol. **124**, 105983 (2020).
36. R. Beuton, B. Chimier, J. Breil, D. Hébert, K. Mishchik, J. Lopez, P. H. Maire, and G. Duchateau, "Thermo-elasto-plastic simulations of femtosecond laser-induced multiple-cavity in fused silica," Appl. Phys. A Mater. Sci. Process. **124**(4), 0 (2018).
37. R. Beuton, B. Chimier, J. Breil, D. Hébert, P. H. Maire, and G. Duchateau, "Thermo-elasto-plastic simulations of femtosecond laser-induced structural modifications: Application to cavity formation in fused silica," J. Appl. Phys. **122**(20), (2017).
38. P. Agostini and G. Petite, "Photoelectric effect under strong irradiation," Contemp. Phys. **29**(1), 57–77 (1988).
39. J. Siegel, D. Puerto, W. Gawelda, G. Bachelier, J. Solis, L. Ehrentraut, and J. Bonse, "Plasma formation and structural modification below the visible ablation threshold in fused silica upon femtosecond laser irradiation," Appl. Phys. Lett. **91**(8), 1–4 (2007).
40. Nye J. F., *Physical Properties of Crystals* (Oxford University Press Inc., 1957).
41. T. N. Vasudevan and R. S. Krishnan, "Dispersion of the stress-optic coefficient in glasses," J. Phys. D. Appl. Phys. **5**(12), 2283–2287 (1972).
42. O. Koritsoglou, D. Loison, O. Uteza, and A. Mouskeftaras, "Characteristics of femtosecond laser-induced shockwaves in air," Opt. Express **30**(21), 37407 (2022).
43. H. Hu, X. Wang, H. Zhai, N. Zhang, and P. Wang, "Generation of multiple stress waves in silica glass in high fluence femtosecond laser ablation," Appl. Phys. Lett. **97**(2010), 061117 (2010).
44. W. P. Mason and H. J. Mcskimin, "Attenuation and Scattering of High Frequency Sound Waves in Metals and Glasses," J. Acoust. Soc. Am. **19**(3), 464–473 (1947).

45. I. M. Burakov, N. M. Bulgakova, R. Stoian, A. Mermillod-Blondin, E. Audouard, A. Rosenfeld, A. Husakou, and I. V. Hertel, "Spatial distribution of refractive index variations induced in bulk fused silica by single ultrashort and short laser pulses," J. Appl. Phys. **101**(4), (2007).
46. R. Stoian, K. Mishchik, G. Cheng, C. Mauclair, C. D'Amico, J. P. Colombier, and M. Zamfirescu, "Investigation and control of ultrafast laser-induced isotropic and anisotropic nanoscale-modulated index patterns in bulk fused silica," Opt. Mater. Express **3**(10), 1755 (2013).
47. S. Juodkazis, K. Nishimura, S. Tanaka, H. Misawa, E. G. Gamaly, B. Luther-Davies, L. Hallo, P. Nicolai, and V. T. Tikhonchuk, "Laser-Induced Microexplosion Confined in the Bulk of a Sapphire Crystal: Evidence of Multimegabar Pressures," Phys. Rev. Lett. **96**(16), 166101 (2006).
48. M. K. Bhuyan, M. Somayaji, A. Mermillod-Blondin, F. Bourquard, J. P. Colombier, and R. Stoian, "Ultrafast laser nanostructuring in bulk silica, a "slow" microexplosion," Optica **4**(8), 951 (2017).
49. A. Mouskeftaras and Y. Bellouard, "Effect of the combination of femtosecond laser pulses exposure on the etching rate of fused Silica in hydrofluoric acid," J. Laser Micro Nanoeng. **13**(1), 26–30 (2018).
50. A. Rudenko, J. V. Moloney, and P. Polynkin, "Ionization clamping in ultrafast optical breakdown of transparent solids," Phys. Rev. Appl. **20**(6), 064035 (2023).